

RAYLEIGH-TAYLOR INSTABILITY IN A RELATIVISTIC FIREBALL ON A MOVING COMPUTATIONAL GRID

PAUL C. DUFFELL AND ANDREW I. MACFADYEN

Center for Cosmology and Particle Physics, New York University

Draft version March 1, 2013

ABSTRACT

We numerically calculate the growth and saturation of the Rayleigh-Taylor instability caused by the deceleration of relativistic outflows with Lorentz factor $\Gamma = 10, 30$, and 100 . The instability generates turbulence whose scale exhibits strong dependence on Lorentz factor, as only modes within the causality scale $\Delta\theta \sim 1/\Gamma$ can grow. We develop a simple diagnostic to measure the fraction of energy in turbulent eddies and use it to estimate magnetic field amplification by the instability. We estimate a magnetic energy fraction $\epsilon_B \sim 10^{-2}$ due to Rayleigh-Taylor turbulence in a shock-heated region behind the forward shock. The instability completely disrupts the contact discontinuity between the ejecta and the swept up circumburst medium. The reverse shock is stable, but is impacted by the Rayleigh-Taylor instability, which strengthens the reverse shock and pushes it away from the forward shock. The forward shock front is unaffected by the instability, but Rayleigh-Taylor fingers can penetrate about 10% of the way into the energetic region behind the shock during the two-shock phase of the explosion. We calculate afterglow emission from the explosion and find the reverse shock emission to be significantly altered by the instability. The reverse shock emission peaks at a later time but is still distinguishable from the forward shock. These calculations are performed using a novel numerical technique that includes a moving computational grid. The moving grid is essential as it maintains contact discontinuities to high precision and can easily evolve flows with Lorentz factors upwards of 300.

Subject headings: hydrodynamics – methods: numerical – relativity

1. INTRODUCTION

In the fireball model (Paczynski 1986; Goodman 1986), gamma ray bursts are thought to be generated by a hot explosion which expands and compresses itself into a thin ultrarelativistic shell. Internal collisions of such shells are thought to generate the prompt burst of gamma rays, after which afterglow emission is produced during the further expansion of the shell. Eventually this shell transfers its energy into a relativistic blastwave propagating into the circumburst medium. During the transfer process there is an interesting phase of the evolution, during which the shell is unstable to the Rayleigh-Taylor instability.

The instability requires a density gradient, for example at the interface between two fluids of different density. In this case, the two fluids are the material contained in the original explosion (the ejecta) and the ambient gas swept up by the explosion (the circumburst medium). Once the explosion has begun to sweep up a non-negligible amount of mass, two shocks form. One of the shocks drives its way forward into the ambient gas, and the other back into the ejecta. Between the two shocks resides the contact discontinuity, marking the separation between ambient gas and ejecta. It is this contact discontinuity which is unstable.

The instability should have some observable signatures. This is primarily due to its impact on the reverse shock, which might be observable in the afterglow radiation from the burst, or perhaps even in the prompt emission. The dynamics of the Rayleigh-Taylor instability should be taken into account in order to accu-

rately predict the magnitude and frequency of the so-called “optical flash” associated with the reverse shock. Additionally, if the instability generates enough shear to cascade into Kelvin-Helmholtz turbulence, this could amplify magnetic fields which facilitate synchrotron emission. Finally, it is unknown whether Rayleigh-Taylor fingers might propagate all the way up to the forward shock (Levinson 2009a), possibly altering the fundamental dynamics of the shock, which are generally thought to be governed by the Blandford-McKee solution (Blandford & McKee 1976) in the ultrarelativistic limit.

These considerations motivate the calculation of the growth of the Rayleigh-Taylor instability in the physical context of a relativistic fireball. The nonrelativistic case was first treated by Chevalier et al (1992), who analytically calculated the linear growth rate of the instability, and also explored numerically its linear growth and nonlinear saturation. Jun & Norman (1996) later performed a two-dimensional magnetohydrodynamics calculation which demonstrated how magnetic fields tend to align themselves along Rayleigh-Taylor fingers.

The relativistic case is relevant for gamma ray bursts, which have Lorentz factors $\Gamma \gtrsim 100$, and relativistic effects should qualitatively change the physics of the instability. First, the growth rate is modified by time dilation (Wang et al 2002). Secondly, causality arguments dictate which modes grow and saturate during different phases of evolution, analogous to the growth of structure in cosmology. Additionally, any turbulence being generated is relativistic turbulence, which may have distinct properties from nonrelativistic turbulence (Zrake & MacFadyen 2012). Finally, while the

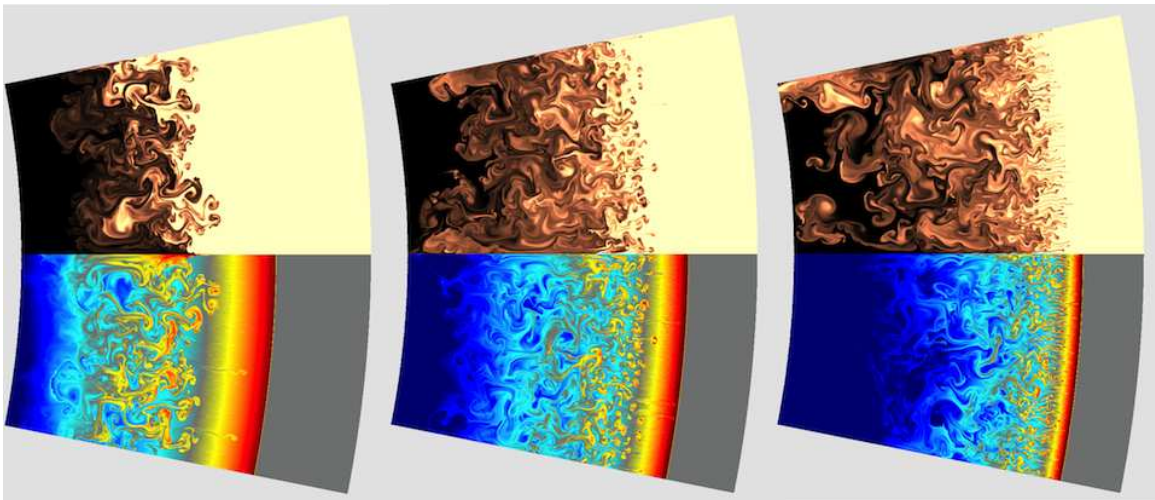


FIG. 1.— The structure of the turbulence strongly depends on relativistic effects. When the energy per mass Γ is varied (the characteristic Lorentz factor of the initial shell), this affects the scale and prominence of Rayleigh-Taylor turbulence. This is a snapshot at $t = t_M$ for $\Gamma = 10, 30$, and 100 . On the lower part of the figure, we plot logarithm of density, while on the upper part we plot a passive scalar which tracks the growth of the instability. The dominant mode is of order the relativistic causality scale $\Delta\theta \sim 1/\Gamma$.

Sedov-Taylor solution is a fast attractor, the relativistic Blandford-McKee solution is a slow attractor (Gruzinov 2000). Any deviation from Blandford-McKee due to Rayleigh-Taylor fingers might persist until the shock becomes nonrelativistic.

To extend the nonrelativistic results into the relativistic regime, Levinson (2009b) performed a stability analysis on the two-shock solution (Nakamura & Shigeyama 2006) and found linear growth rates which could potentially be large enough to impact the forward shock.

In this work, we evolve a relativistic fireball numerically in 2D, to calculate its dynamics, and to explore the consequences of this instability to observations of gamma ray bursts and their afterglows. We study in detail how the qualitative features of turbulence are changed by relativistic effects (Figure 1), and we describe generally how the dynamics of the two-shock system are affected. To improve code performance, we use a moving numerical mesh, which follows the radial motion of the bulk flow and reduces the advection errors associated with this motion. Doing this results in a vastly improved calculation of the shock dynamics, and an increased sensitivity to the subtle effects that must be captured. The code is also able to perform calculations with large Lorentz factors ($\Gamma \gtrsim 100$), which allows us to probe astrophysically relevant regions of parameter space.

2. METHOD

We solve the relativistic hydrodynamics equations:

$$\partial_\mu(\rho u^\mu) = 0 \quad (1)$$

$$\partial_\mu((\rho + 4P)u^\mu u^\nu + Pg^{\mu\nu}) = 0 \quad (2)$$

where ρ is the proper mass density, P is the pressure, and u is the four velocity. We use units for which $c = 1$. We also evolve a passive scalar field, X , according to

$$\partial_\mu(\rho X u^\mu) = 0. \quad (3)$$

This allows us to track the growth of the instability, demarking which fluid elements are in the ejecta and which are in the circumburst medium. We set $X = 0$ for the

ejecta behind the contact discontinuity, and $X = 1$ for the ambient gas in front.

2.1. Numerics

The numerical method we employ is a variant of the TESS method (Duffell & MacFadyen 2011) with specific application to problems involving rapid radial outflow.

TESS is a finite-volume, moving-mesh hydrodynamics method which in its original form constructs its numerical mesh from a Voronoi tessellation of the computational domain. The computational zones move with the local fluid velocity, and change their shape and size as they move and shear past one another. In this sense, the method is effectively Lagrangian.

This idea can be improved if the moving mesh is not generated from a Voronoi tessellation, but instead is specifically tailored to a given flow. Most of the numerical benefits from TESS do not come from the Voronoi tessellation, but from the simple fact that cells are allowed to move. This enables resolution of contact discontinuities to very high precision, and potentially allows for much longer timesteps. By moving the mesh, but choosing a particular shape for grid cells (other than Voronoi), the code can be adapted to the problem at hand.

The TESS method defines its numerical mesh abstractly, so that all that is required to take into account a given mesh topology are the positions and volumes of computational zones, and the positions and areas of “faces”, which are simply defined to be any boundary between two zones. This means more specific mesh topologies can be generated without changing anything fundamental about the method.

We have previously made this adaptation for Keplerian flow in a gaseous disk (Duffell & MacFadyen 2012). In that case, instead of Voronoi cells, the cells were chosen to be wedge-like annular segments like those of a standard polar grid, and they rotated with the local orbital velocity. We now specifically refer to the shearing-disk version as the DISCO code.

In this work, we take a similar approach, but instead adapt the grid to a radial outflow, such as a jet. The

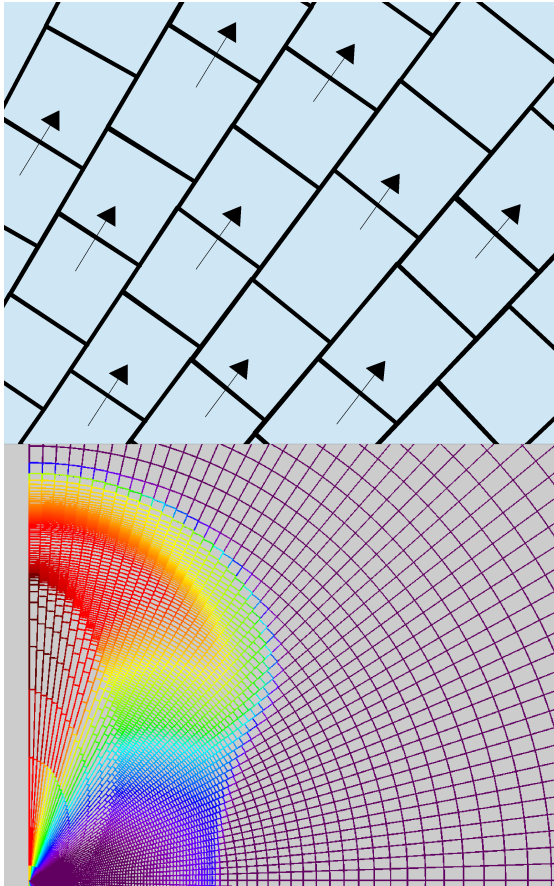


FIG. 2.— The numerical grid shears with the radial velocity of the gas. Each radial track moves independently, each behaving essentially as a 1D lagrangian code. The upper panel shows the motion of grid cells, and the lower panel shows the shearing grid being employed to follow a jet-like explosion.

wedge-like annular shape is still employed, but instead of rotating, the grid expands and shears radially (Figure 2). The numerics are nearly identical to DISCO; we have merely changed the direction of grid motion. By moving the mesh radially instead of azimuthally, the code effectively behaves as a series of one-dimensional Lagrangian codes, coupled laterally by transverse fluxes. The moving grid helps to capture the growth of the instability, and it also allows accurate calculations for large Lorentz factors $\Gamma \gtrsim 100$.

We integrate the equations in two dimensions assuming axisymmetry. The computational domain consists of an angular wedge $0 < \theta < \pi/16$. We use an angular resolution $N_\theta = 1600$ and a resolution in the radial dimension of $N_R \sim 12800$, which were chosen for a resolution of $\Delta\theta \sim \Delta r/r \sim 10^{-4}$. The number of radial zones varies throughout the course of the calculation, because zones are added and removed from the computational domain as necessary during the course of the calculation. The aspect ratio of a typical computational zone is of order unity, but if a cell becomes too long or short, the grid is dynamically refined or de-refined by splitting or merging zones. Aspect ratios in general range between 5 and $1/5$. The inner and outer radial boundaries of the domain can also move during the time integration, so that only fraction of the dynamical range must be covered at any one time.

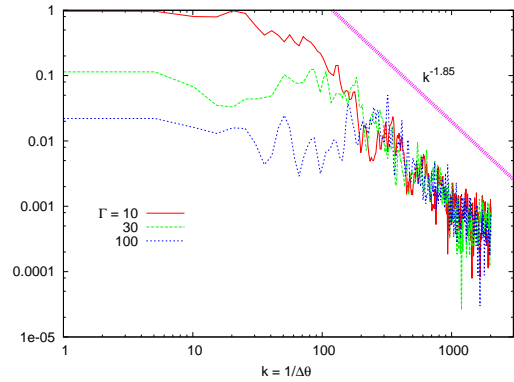


FIG. 3.— The power spectrum of the Rayleigh-Taylor for the three examples shown in Figure 1. Curves are calculated by measuring the Fourier transform of $\delta r/r$ in front of the Rayleigh-Taylor instability. There is a break in the power spectrum at the causality scale $\Delta\theta \sim 1/\Gamma$.

2.2. Initial Conditions

The calculation begins with a hot explosion with a given energy E and mass M with characteristic Lorentz factor $\Gamma \equiv E/M$, within a negligibly small radius, in a cold uniform-density medium with density ρ_0 . This specifies the problem completely, provided we have a definition for “negligibly small radius”. The initial radius R_0 of the explosion must be small enough that the “coasting phase” at $t \sim \Gamma R_0$ and the “spreading phase” at $t \sim \Gamma^2 R_0$ occur long before the shell begins to decelerate, at the deceleration time

$$t_\gamma = \left(\frac{M}{\Gamma \rho_0} \right)^{1/3}. \quad (4)$$

In this limit ($\Gamma^2 R_0 \ll t_\gamma$), the initial structure of the fireball has no effect on what happens after $t > t_\gamma$ (we have checked this empirically). This is the so-called “thin-shell” limit. At $t = t_\gamma$, the shell decelerates, which causes the formation of the forward and reverse shocks. This generates a self-similar solution which persists until $t = t_M$, where

$$t_M = (M/\rho_0)^{1/3}. \quad (5)$$

During this phase of expansion, between t_γ and t_M , the Rayleigh-Taylor instability is most significant.

To capture the first phases of evolution, we evolve the explosion in one dimension from the initial fireball until a time $t < t_\gamma$, when the mass in the forward shock is still a small fraction of the mass of the ejecta. Then the code is switched to evolve the system in 2D, to capture the growth of the instability. At this point, we also set the value of X on either side of the blast wave ($X = 0$ behind and $X = 1$ in front). The initial parameters are E , M , and ρ_0 , but due to scale invariance, in this thin-shell limit the only parameter which must be varied is the energy per unit mass in the fireball, $E/M = \Gamma$. Thus all the parameter space of this problem is reduced to this single variable. In this study, we use values of $\Gamma = 10, 30$, and 100 . We have also performed calculations with $\Gamma = 300$ but resolution was insufficient to correctly evolve the instability. The $\Gamma > 100$ case will be presented in a future work.

In principle, the instability grows from some seed perturbations which break the spherical symmetry of the

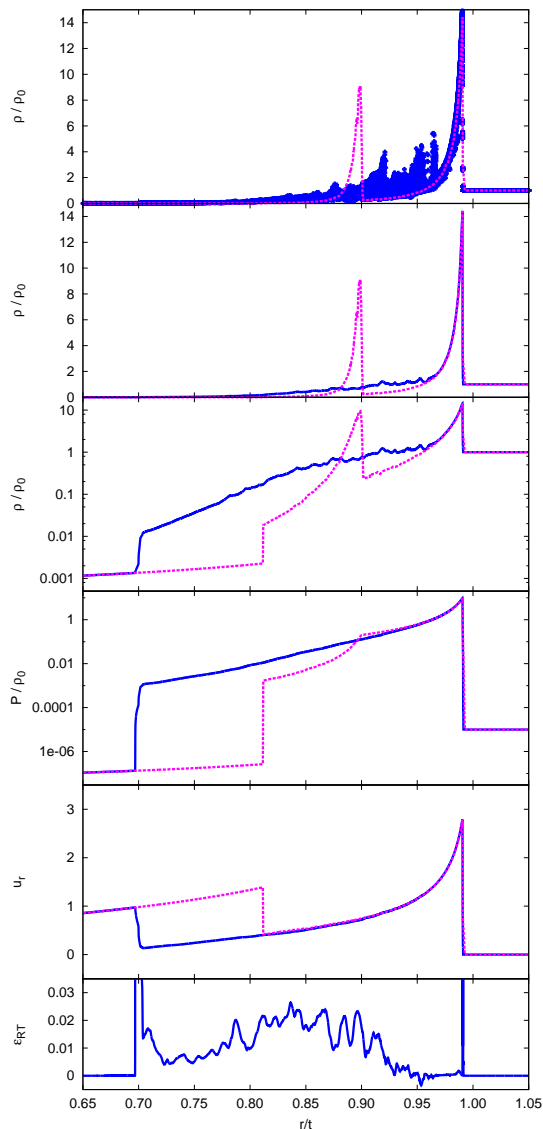


FIG. 4.— The same calculation has been performed in 2D assuming axisymmetry, and in 1D assuming spherical symmetry. The instability is present in two dimensions, and has a clear impact on the spherically averaged fields. This is a snapshot of proper density at $t = t_M$ for $\Gamma = 30$, comparing the 1D and 2D solutions. The top panel shows the scatter of density present in two dimensions, compared to the two-shock solution with sharp contact discontinuity found in 1D. The second panel shows an angular average of the two-dimensional field, which demonstrates that the contact discontinuity is completely disrupted. Panels 3-5 show a logscale profile in density, pressure and Lorentz factor, showing clearly the position of the reverse shock, which is pushed back by the instability. The bottom panel shows the turbulent energy fraction, ϵ_{RT} (§3.2).

initial conditions. However, we found that for weak enough perturbations the saturated instability does not depend (in a statistical sense) on how the perturbations are seeded. This includes the limit where there are no explicit perturbations, but the instability is seeded with numerical noise, which is extremely small but still large enough to break the symmetry. All calculations performed here did not use explicit perturbations to seed the instability.

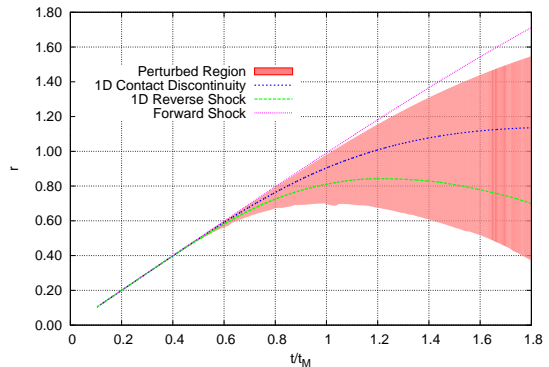


FIG. 5.— Another comparison between the one-dimensional and two-dimensional versions of this experiment, for $\Gamma = 30$. In this figure we plot the positions of the characteristic waves present within the shell. The forward shock is unaffected by the instability, the contact discontinuity is sheared out into the large shaded region, and the reverse shock is pushed away from the forward shock.

3. RESULTS

In Figure 1 we demonstrate how relativistic effects can affect the character of Rayleigh-Taylor turbulence. We show a snapshot at $t = t_M$ for various values of $\Gamma = E/M$, which is roughly a proxy for the initial Lorentz factor. For larger Lorentz factors, the fastest growing modes can be found on smaller angular scales. This has to do with causality; the saturated instability favors large-scale modes, but there is a large-scale cutoff given by the horizon scale, $\Delta\theta \sim 1/\Gamma$. Modes larger than this scale do not grow. This is most explicitly shown in the power spectrum of the contact discontinuity, which we have plotted in Figure 3. The perturbation also propagates further both upstream and downstream for larger values of Γ . For the turbulence moving back into the ejecta this is due to increased pressure and density gradients in the unstable region. For the forward-propagating turbulence, it is due to the fact that the gas is compressed into a thin shell $\sim r/\Gamma^2$ behind the forward shock, and the width of this shell decreases with Γ .

3.1. 1D vs 2D

The primary effects of the Rayleigh-Taylor instability on the shock dynamics are displayed in Figure 4. This is a snapshot of the shockwave at $t = t_M$ for $\Gamma = 30$. We show the radial profile and compare it with the same calculation performed in 1D assuming spherical symmetry. In the 1D case, we see the standard two-shock solution which has been extensively used to describe GRB phenomenology.

From this figure, the most obvious distinction between one and two dimensions is the complete disruption of the contact discontinuity in 2D, which of course is expected since it is the contact discontinuity which is unstable. The second plainly visible distinction here is in the reverse shock. Clearly in the 2D case, the instability has managed to perturb the reverse shock, and this has altered the shock's characteristic speed. In the 2D case, the reverse shock propagates much further back than in 1D. This apparently does not happen to the forward shock, as it remains undisturbed. It is possible that this conclusion could be challenged by a three dimensional calculation, but we do not expect this to be the case, as the instability

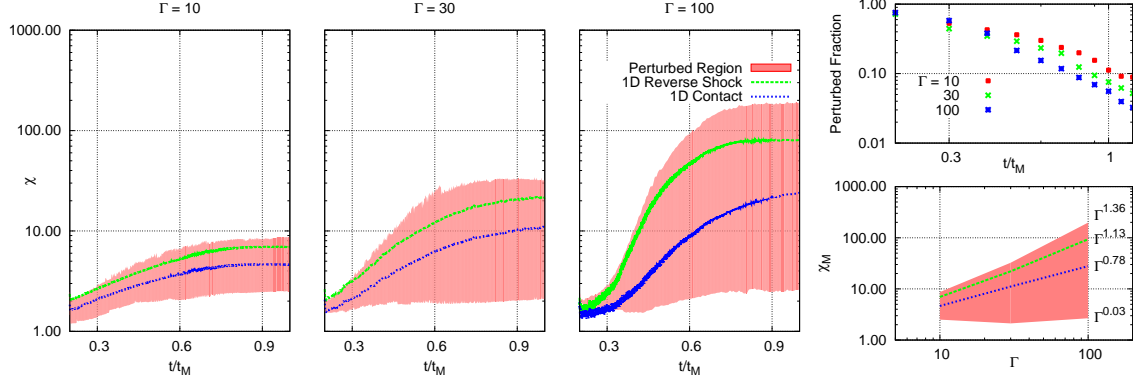


FIG. 6.— The fireball converts itself from a thin shell into the two-shock structure, and as $t \rightarrow t_M$ the characteristic waves obey self-similarity. This remains true for the unstable 2D version of the problem. Here we have plotted the position of the characteristic waves in terms of the self-similarity variable, χ (Eq. 6). Shortly after $t = t_M$, the characteristic waves fall behind the shock. In the upper right panel we show the fraction of energy which is perturbed by the instability, roughly 10% at $t = t_M$. In the lower right panel we show how the position of characteristic waves scales with Lorentz factor.

would dissipate more efficiently in 3D.

Characteristic waves are shown in Figure 5, where we compare 1D and 2D shock dynamics. Here again, we can see important effects of the instability: What was a contact discontinuity becomes smeared over a larger region in 2D, overtaking the reverse shock but leaving the forward shock alone.

We can compare different values of Γ on a similar footing by expressing the positions of characteristic waves in terms of the self-similarity parameter,

$$\chi = \frac{1 - r/t}{1 - r_{\text{shock}}/t}. \quad (6)$$

We plot the value of χ for all characteristic waves in Figure 6 for $\Gamma = 10, 30$, and 100 . As $t \rightarrow t_M$, the characteristic waves approach constant values of χ . From these three examples, it appears that the forward position of the Rayleigh-Taylor fingers approaches a value of $\chi \sim 2.5$ which is independent of Γ . We might expect from this that turbulence should be present in about one third of the energy behind the shock, though in practice we find this fraction is closer to 10%. This is the percentage which is turbulent and therefore magnetized by Rayleigh-Taylor (we calculate the magnetization in §3.2). After $t = t_M$, the shock moves away from the fingers quickly and have no further impact on the forward shock dynamics.

3.2. Turbulence

It will be useful to measure the kinetic energy of large eddies in the turbulent region of the solution, since that will provide insight into the turbulent cascade which would take place in a highly-resolved 3D calculation. It turns out that the relevant quantity, the turbulent energy fraction,

$$\epsilon_{RT} = \frac{\text{Turbulent Kinetic Energy}}{\text{Thermal Energy}} \quad (7)$$

can be measured in a relatively simple manner. In our analysis, we have converted 2D data into 1D data by averaging in a conservative way. That is, for a given radial annulus, the total mass, energy, and momentum of that annulus are calculated, and from these quantities

the conservatively averaged density, pressure, and four velocity are determined (this is how the middle panels of Figure 4 were generated). We note that this averaging process typically results in a slightly larger pressure than would result from arithmetically averaging the pressure by volume on an annulus. This is because when the momentum of an annulus is calculated, there is cancellation due to the variations in velocity with angle, and this “lost” kinetic energy is interpreted as thermal energy in the averaged quantities.

In other words, the excess of thermal energy from averaging conservatively over angle is exactly the turbulent kinetic energy contained in that annulus. This provides a very simple means of calculating the fraction of energy in large eddies:

$$\epsilon_{RT} = \frac{\Delta P}{P} \quad (8)$$

where ΔP is the difference between “conservatively averaged” pressure and volume-averaged pressure.

We have plotted a snapshot of ϵ_{RT} in the lower panel of Figure 4. There is clearly variation with radius, but in this snapshot it roughly peaks around $\epsilon_{RT} \sim 0.02$. For the three cases studied, this turbulent fraction peaks at time $t \sim t_M$ with this same peak value, roughly independent of Γ .

This turbulent energy is free to cascade to smaller scales (as it would in a 3D calculation) and to amplify magnetic fields (as it would if magnetic fields were included in our calculation). In fact, it is straightforward to estimate the saturated magnetic energy fraction, because it has been shown (Zhang et al 2009; Zrake & MacFadyen 2013) that it is roughly in equipartition with the turbulent kinetic energy:

$$\epsilon_B \sim \epsilon_{RT} \sim 10^{-2}. \quad (9)$$

This is the magnetization induced by Rayleigh-Taylor alone, though magnetic fields could be amplified by other mechanisms.

3.3. Afterglow Emission

We have calculated light curves in one and two dimensions, in order to explore the observational consequences of the instability. Relativistic Doppler effects

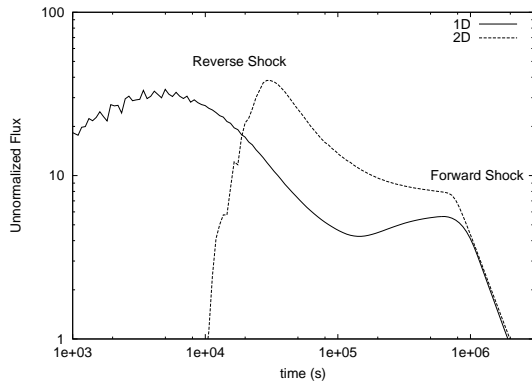


FIG. 7.— The reverse shock is directly observed in the early afterglow emission. We plot microwave light curves for $\Gamma = 30$ for the 1D (stable) and 2D (unstable) versions of the problem. The second peak is due to the forward shock, which is unaffected by the instability. The first peak is emission from the reverse shock. This flash occurs at a later time and the peak is narrower. are responsible for the hard gamma-ray and X-ray afterglow emission, but the reverse shock generally has a much lower Lorentz factor than the forward shock, so it cannot compete with the forward shock at high frequencies. At lower frequencies (optical, microwave, radio) the flux from the forward and reverse shocks can be comparable, so in these wavelengths we search for observational signatures of the Rayleigh-Taylor instability.

By implementing a simple model for synchrotron emission directly into the hydrodynamical evolution, we calculate a microwave light curve for our $\Gamma = 30$ model. We calculate the flux from a given computational zone at a given observer time from the formula:

$$F \propto \frac{\rho B}{\gamma^2(1 - v_z)^2} Q(\nu) \quad (10)$$

where the magnetic energy is assumed to be proportional to the thermal energy,

$$B \propto \sqrt{P} \quad (11)$$

and frequency dependence assumes “slow cooling”

$$Q(\nu) = \begin{cases} (\nu/\nu_m)^{1/3} & \nu < \nu_m \\ (\nu/\nu_m)^{(1-p)/2} & \nu > \nu_m \end{cases} \quad (12)$$

where we choose $p = 2.5$, and where ν_m is the characteristic synchrotron frequency,

$$\nu_m \propto B(P/\rho)^2 \quad (13)$$

This is a simplified version of the emission model in Van Eerten et al (2010).

We show the light curve in Figure 7 for $\Gamma = 30$. To single out signatures of Rayleigh-Taylor, we compare 1D and 2D results. The forward shock emission is unaffected, as the forward shock is not perturbed by the instability. The reverse shock emission is affected by the instability; the peak magnitude is not diminished significantly, but the peak occurs at a later time in 2D than in 1D.

4. SUMMARY

We have computed the development and saturation of Rayleigh-Taylor instability in relativistic fireballs using a moving computational mesh. The instability does not perturb the forward shock, but it completely disrupts

the contact discontinuity between the ejecta and the surrounding medium, and it significantly modifies the dynamics of the reverse shock, which may cause reverse shock emission to peak at a later time. The relativistic shear flow generated by Rayleigh-Taylor fingers may also provide a site for cosmic ray acceleration.

The Rayleigh-Taylor instability is effective in stirring up turbulence; we find that turbulent kinetic energy reaches about 1% of thermal energy wherever the turbulence is present, which should rapidly amplify magnetic fields up to 1% of thermal by the operation of small-scale dynamo (Zrake & MacFadyen 2013) during the deceleration phase (between t_γ and t_M). The turbulence is present in a region behind the forward shock, but Rayleigh-Taylor fingers attempt to reach out towards this shock, penetrating about 10% of its energy. The reverse shock is impacted immediately, and it is pushed away from the forward shock, strengthening it and causing its emission to be observed at a later time. This motivates 3D calculations, as these numbers might change when 3D turbulence effects are taken into account.

This emphasizes the importance of accounting for fluid instabilities when considering the dynamics and observational signatures of gamma ray bursts. Figure 4 gives some hope that an effective 1D description of the dynamics may be possible; adding some kind of diffusive term in 1D to shocked fluid elements in the ejecta, for example, might reproduce physical profiles close to those in Figure 4.

This motivates a more comprehensive study which includes more general circumburst profiles, larger Lorentz factors (converged results with $\Gamma \sim 300$ or higher are much more computationally intensive but certainly possible), and potentially 3D turbulence effects. Because of scale invariance, our only free parameter is Γ , the characteristic Lorentz factor. The dynamics and synchrotron emission both can be re-scaled to arbitrary explosion energy and circumburst density, which means that a suite of calculations for different values of Γ will completely cover the parameter space of all such explosions (Van Eerten & MacFadyen 2012; Granot 2012). This motivates us to implement a detailed synchrotron emission model (Van Eerten et al 2010), to perform a comprehensive study of emission from GRB outflows. All of this is planned as future work.

This research was supported in part by NASA through grants NNX10AF62G and NNX11AE05G issued through the Astrophysics Theory Program and by the NSF through grant AST-1009863.

Resources supporting this work were provided by the NASA High-End Computing (HEC) Program through the NASA Advanced Supercomputing (NAS) Division at Ames Research Center. We are grateful to Jonathan Zrake for helpful comments and discussions.

REFERENCES

- Blandford, R. D. & McKee, C. F. 1976, *Phys. Fluids*, 19, 1130
 Chevalier, R. A., Blondin, J. M. & Emmering, R. 1992, *ApJ*, 392, 118
 Duffell, P. C. & MacFadyen, A. I. 2011, *ApJS*, 197, 15
 Duffell, P. C. & MacFadyen, A. I. 2012, *ApJ*, 755, 7
 Goodman, J. 1986, *A&A*, 308, L47
 Goodman, J. & MacFadyen, A. I. 2008, *J. Fluid Mech.*, 604, 325
 Granot, J. 2012, *MNRAS*, 421, 2610
 Gruzinov, A. 2000, *arXiv:astro-ph/0012364*
 Jun, B. I. & Norman, M. L. 1996, *ApJ*, 465, 800
 Levinson, A. 2009a, *ApJ*, 705, L213
 Levinson, A. 2009b, *Geophysical & Astrophysical Fluid Dynamics*, 104, 85
 Nakamura, K. & Shigeeyama, T. 2006, *ApJ*, 645, 431
 Paczynski, B. 1986, *A&A*, 308, L43
 Van Eerten, H., Zhang, W. & MacFadyen, A. I. 2010, *ApJ*, 722, 235
 Van Eerten, H. & MacFadyen, A. I. 2012, *ApJ*, 747, L30
 Wang, X., Loeb, A. & Waxman, E. 2002, *ApJ*, 568, 830
 Zhang, W., MacFadyen, A. I., & Wang, P. 2009, *ApJ*, 568, 830
 Zrake, J. & MacFadyen, A. I. 2012, *ApJ*, 744, 32
 Zrake, J. & MacFadyen, A. I. 2013 (in press)